Field-dependent anisotropic room-temperature ferromagnetism in Cr₃Te₄

Aina Wang [1,2] Azizur Rahman [2,*] Zan Du [1,2] Jun Zhao,[1,3] Fanying Meng,[1,2] Wei Liu,[4]
Jiyu Fan,[5] Chunlan Ma [6] Min Ge,[2] Li Pi,[1,2,7] Lei Zhang [1,7,†] and Yuheng Zhang[1,2,7]

[1]*Anhui Key Laboratory of Condensed Matter Physics at Extreme Conditions, High Magnetic Field Laboratory,*
Hefei Institutes of Physical Science, Chinese Academy of Sciences, Hefei 230031, China
[2]*Hefei National Laboratory for Physical Sciences at the Microscale, University of Science and Technology of China, Hefei 230026, China*
[3]*School of Mechanical and Electrical Engineering, Sanming University, Sanming 365004, China*
[4]*Institutes of Physical Science and Information Technology, Anhui University, Hefei 230601, China*
[5]*Department of Applied Physics, Nanjing University of Aeronautics and Astronautics, Nanjing 210016, China*
[6]*Jiangsu Key Laboratory of Micro and Nano Heat Fluid Flow Technology and Energy Application,*
School of Physical Science and Technology, Suzhou University of Science and Technology, Suzhou 215009, China
[7]*The High Magnetic Field Laboratory of Anhui Province, Hefei 230031, China*

Materials hosting intrinsic room-temperature ferromagnetism have significant application in spintronics. In this context, the transition metal sulfide chromium telluride (Cr_xTe_y) has sparked significant attention due to its room-temperature ferromagnetism, as well as high magnetic anisotropy, easy tunability, and air stability. This study carefully examines the magnetic characteristics of an intrinsic room-temperature ferromagnetic Cr₃Te₄ single crystal. Magnetization measurements identify a paramagnetic-to-ferromagnetic (PM-FM) phase transition at $T_C \sim 322$ K and high magnetic anisotropy. Meanwhile, a coexistence of ferromagnetism and antiferromagnetism is unveiled below $T_N \sim 90$ K. A systematic investigation of magnetization isotherms collected near T_C provides the asymptotic critical exponents $\beta = 0.365(5)$, $\gamma = 1.212(9)$, $\delta = 4.580(4)$ for $H//ab$, and $\beta = 0.370(3)$, $\gamma = 1.329(1)$, $\delta = 4.554(9)$ for $H//c$. The obtained critical exponents for $H//ab$ and $H//c$ suggest strong anisotropic and multiple magnetic interactions in Cr₃Te₄. The comprehensive $H - T$ phase diagrams for $H//ab$ and $H//c$ are constructed using universal scaling and detailed magnetization, revealing strong field-dependent anisotropic room-temperature ferromagnetism and coexistence of ferromagnetism, antiferromagnetism, and noncollinear ferromagnetism. The multiple phases demonstrate that the magnetic couplings in Cr₃Te₄ are mediated by intralayer super exchange, interlayer double exchange, and direct exchange.

I. INTRODUCTION

The finding of intrinsic long-range magnetic ordering in two-dimensional (2D) materials sparks interest in low-dimensional magnetism and opens the door to spintronics applications. According to the Mermin-Wagner theorem, long-range magnetic order cannot exist in a 2D isotropic Heisenberg system due to the strong thermal fluctuation [1]. However, strong anisotropy can suppress the thermal fluctuation, leading to long-range magnetic ordering in a 2D system [1]. Intrinsic long-range magnetic ordering is respectively found in monolayered CrI₃ [2] and bilayered Cr₂Ge₂Te₆ [3], which opens the opportunity to low-dimensional magnetism. Subsequently, in Fe₃GeTe₂ with Curie temperature $T_C \sim 205$ K, long-range ferromagnetism is revealed to be maintained until monolayer, which can be modulated to room temperature by the ionic gate method [4]. Theoretical studies predict that intrinsic ferromagnetic order may also exist in other systems, such as monolayered Cr₂Si₂Te₆ with $T_C \sim$

33 K for bulk crystals [5,6]. However, these materials are very unstable in air and T_C is much lower than the room temperature, especially for the monolayered or few-layered samples, significantly hindering their applications.

Chromium telluride Cr_xTe_y, a transition metal sulfide family of materials, has received a lot of interests for its easy tunability, room-temperature ferromagnetism, strong magnetic anisotropy, and air stability [7–9]. For example, intrinsic ferromagnetism has been observed in ultrathin CrTe crystals, which are non van der Waals (vdW) structures but still can be exfoliated due to the low cleavage energy of (002) face [10]. The T_C of 2D CrTe (~ 367 K) is higher than that of a bulk (~ 343 K) crystal, both of which are above room temperature [10]. The crystal structure of Cr_xTe_y can be tuned by stoichiometry, pressure, and field. Corresponding changes in conductivity and magnetism occur simultaneously [11–14]. Many materials in this family have been reported to have near-room-temperature T_C and tunable magnetism, including 1T-CrTe₂ (~ 320 K) [15], Cr₅Te₈ (~ 230 K for trigonal and ~ 222 K for monocline) [16,17], Cr₃Te₄ (~ 316 K) [18], Cr₄Te₅ (~ 318 K) [19], and Cr₅Te₆ (~ 338 K) [20]. Additionally, a topological Hall effect has been detected in Cr_xTe_y, suggesting the presence of topological or noncollinear

*Corresponding author: aziz@mail.ustc.edu.cn
†Corresponding author: zhanglei@hmfl.ac.cn

magnetic structures such as skyrmions in CrTe single crystals and Cr_2Te_3-Bi interface, bi-skyrmions in Cr_3Te_4, and Moiré superlattice in Cr_5Te_8 heterostructure [9,21–29]. In particular, the bi-skyrmion in Cr_3Te_4 is suggested to promote the development of a new generation of high-density memory functions, whereas the spin filtering effect in Cr_3Te_4 can further show its superiority in spintronic device application [30]. In addition, for atomic-thick Cr_3Te_4, previous studies have unveiled that the Curie temperature and the magnetocrystalline anisotropy are strongly dependent on the layer numbers [31,32].

Although many theoretical and experimental studies have been carried out on 2D Cr_3Te_4 [29,31,32], however, few investigations have been performed for bulk single crystals. Because of the exotic physical properties such as room-temperature ferromagnetism and bi-skyrmion in Cr_3Te_4, magnetic structures must be clarified due to the close relationship between the exotic properties and its magnetism. Therefore, this study thoroughly investigates the magnetism of the Cr_3Te_4 single crystal. The magnetization study suggests that the Cr_3Te_4 single crystal exhibits anisotropic magnetic behaviors with the easy axis in *ab* plane. Using analytical techniques such as modified Arrott plot, Kouvel-Fisher plot, and critical isotherm analysis, critical exponents β, γ, δ are obtained for $H//ab$ and $H//c$. The obtained critical exponents with different field orientations suggest strong anisotropic and multiple magnetic interactions in Cr_3Te_4 single crystal. Furthermore, $H - T$ phase diagrams for $H//ab$ and $H//c$ are constructed, and the magnetic structures are explored. Multiple magnetic interactions, including intralayer super exchange, interlayer double exchange, and direct exchange, are revealed.

II. EXPERIMENTAL METHODS

Single crystals of Cr_3Te_4 were grown by a chemical vapor transport (CVT) method [18]. High-purity powders of Cr (99.99%, Alfa Aesar) and Te (99.99%, Alfa Aesar) were mixed thoroughly in an Ar-filled glove box. The mixture was sealed in an evacuated quartz tube, with iodine used as the transport agent. The quartz tube was heated up slowly to 400°C, and held at that temperature for 24 hours. Then, it was continuously heated to 1000 °C for the source zone and 820 °C for the depositional district. After being held for a week, the quartz tube was cooled to room temperature. Finally, bright single crystals with hexagonal shape can be acquired on the cold side of the tube.

The crystalline structure was checked by the x-ray diffraction (XRD) with Cu Kα radiation using Rigaku-TTR3 diffractometer. The chemical compositions were determined by the energy dispersive x-ray spectrometry (EDXS) in an FEI Nanolab 600i SEM/FIB dual beam system. The magnetic behaviors were measured by a superconductive quantum interference device vibrating sample magnetometer (SQUID-VSM) (MPMS-3, Quantum Design). To acquire the initial isothermal magnetization, the sample was heated above the phase transition temperature. Then, after held for 2 minutes, the sample was cooled to the target temperature under zero field to carry out the isothermal magnetization measurement. The temperature dependence of magnetization [$M(T)$] curves
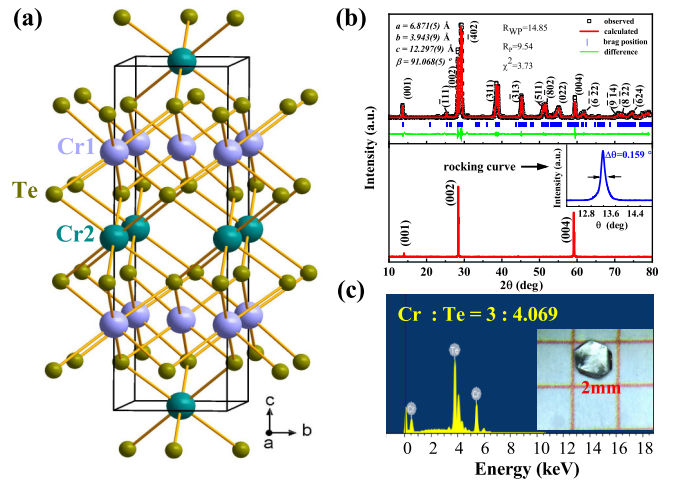

FIG. 1. (a) Crystal structure of Cr_3Te_4. (b) XRD patterns for powder and single-crystal Cr_3Te_4 (the inset shows the rocking curve). (c) EDXS of the single crystal (the inset gives the picture of the as-grown single crystal).

were measured under zero-field cooling (ZFC) and field-cooling (FC) sequences, respectively. The ZFC $M(T)$ curve was obtained by cooling the sample to low temperature under zero field, and then measured on warming under external field. The FC $M(T)$ curve was registered by cooling the sample to low temperature under external field, and then measured on warming under external field.

III. RESULTS AND DISCUSSION

Figure 1(a) illustrates the crystal structure of Cr_3Te_4, which has a monoclinic symmetry with pseudo-NiAs type belonging to the space group $I2/m$ (No.12). Alternatively, Cr_3Te_4 can be regarded as $CrTe_2$ with intercalation of 50% Cr atoms [33,34]. The Cr vacancies are ordered along the *c* axis, where Cr1 and Cr2 represent the fully-occupied and vacant layers, respectively [18,35–37]. Figure 1(b) shows XRD patterns for Cr_3Te_4 powder and single crystal. The powder XRD can be fitted with the space group $I2/m$, which gives the lattice constants $a = 6.871(5)$ Å, $b = 3.943(9)$ Å, $c = 12.297(9)$ Å, and $\beta = 91.068(5)°$. The obtained lattice constants are in agreement with the previous reports [18,35]. The observed Bragg peaks of the single-crystal XRD pattern can be indexed by (00*l*) indices of the lattice plane, suggesting that the *c* axis is perpendicular while the *ab* plane is parallel to the surface of the sample. The inset of Fig. 1(b) displays the rocking curve of the single crystal, which exhibits a single peak with full-width-at-half-maximum (FWHM) of $\Delta\theta = 0.159°$. Figure 1(c) shows the EDXS of the single crystal, which gives the stoichiometry of Cr : Te = 3 : 4.069, highly close to the desired ratios [38]. The picture of the single crystal is presented in the inset of Fig. 1(c), the hexagonal shape of which agrees with the crystal structure. The XRD and EDXS indicate the high quality of the as-grown single crystals.

Figures 2(a) and 2(b) display the $M(T)$ curves for $H//ab$ and $H//c$, respectively. As temperature decreases, a paramagnetic-to-ferromagnetic (PM-FM) transition occurs for both $H//ab$ and $H//c$. The insets of Figs. 2(a) and 2(b)
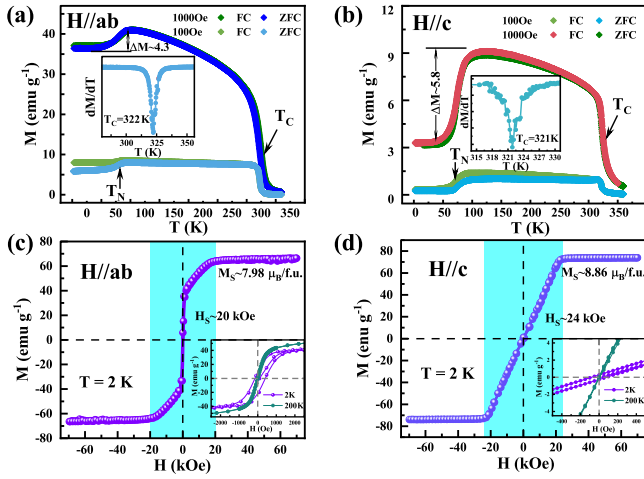
FIG. 2. [(a),(b)] Temperature-dependent magnetization [$M(T)$] for $H//ab$ and $H//c$ (the insets plot dM/dT with $H = 100$ Oe). [(c),(d)] Field-dependent magnetization [$M(H)$] at $T = 2$ K for $H//ab$ and $H//c$ (the insets show the enlarged $M(H)$ curves in low-field region for $T = 2$ K and 200 K).

FIG. 3. [(a),(b)] Initial isothermal $M(H)$ around T_C with $H//ab$ and $H//c$. [(c),(d)] Arrott plot for $H//ab$ and $H//c$.

show the dM/dT curves for $H//ab$ and $H//c$, respectively, where the Curie temperature (T_C) are determined as $T_C^{ab} = 322$ K and $T_C^c = 321$ K by the minimum of dM/dT curves. As the temperature drops, both $M(T)$ curves for $H//ab$ and $H//c$ show a decline at ~ 90 K, indicating another magnetic transition. Under $H = 1000$ Oe, the magnetic steps are $\Delta M \sim 4.3$ emu/g for $H//ab$ and $\Delta M \sim 5.8$ emu/g for $H//c$. In fact, the magnetic transition at 90 K is demonstrated to be an antiferromagnetic (AFM) one, in agreement with the previous reports [18,35].

Furthermore, $M(T)$ curves under ZFC and FC sequences display low-temperature divergence, which may be attributed to canted AFM structures and magnetocrystalline anisotropy [17,39]. $M(T)$ values for $H//ab$ are substantially larger than those for $H//c$, indicating that the easy axis is within the ab plane. It is noticed that the easy axis of a monolayered Cr_3Te_4 is out-of-plane, suggesting that the easy axis can be modified by crystal thickness [31]. The difference between the $M(T)$ curves for is resulted from the magnetic anisotropy. For the magnetic material with strong anisotropy, the direction of applied field usually affects the magnetic behaviors. For Cr_3Te_4, the T_C for $H//ab$ and $H//c$ are identical, which means that the direction of field has rarely effect on the FM transition. However, the heights of the steps at T_N are very different for $H//ab$ and $H//c$, which indicates that the direction of field has a significant influence on the AFM transition temperature. The AFM step for $H//c$ is larger than that for $H//ab$, indicating the enhancement of the AFM transition for $H//c$. The field dependence of magnetization [$M(H)$] measured at $T = 2$ K for $H//ab$ and $H//c$ are shown in Figs. 2(c) and 2(d), respectively. The saturation field and saturation magnetization are determined as $H_S^{ab} \sim 20$ kOe with $M_S^{ab} \sim 7.98$ $\mu_B/f.u.$ for $H//ab$, and $H_S^c \sim 24$ kOe with $M_S^c \sim 8.86$ $\mu_B/f.u.$ for $H//c$, respectively. The enlarged $M(H)$ curves at 2 K and 200 K in the low-field region are shown in the insets of Figs. 2(c) and 2(d). In the low-field region, $M(H)$ for $H//ab$ increases sharply while that for $H//c$ increases gradually,
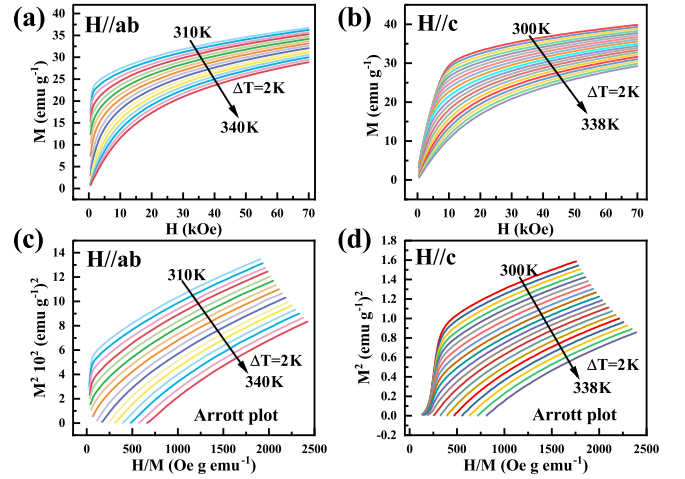
confirming the easy axis along the ab plane for bulk crystals. Moreover, very small loops are observed in low-temperature and low-field regions, which are rarely affected by the phase transitions.

To further explore the magnetic anisotropy and nature of PM-FM transition in Cr_3Te_4, the initial isothermal $M(H)$ curves were measured around T_C. Both initial isothermal $M(H)$ curves for $H//ab$ and $H//c$ reveal saturation behaviors below T_C, as shown in Figs. 3(a) and 3(b). The Arrott plot of M^2 vs H/M can uncover useful information for FM transition. The M^2 vs H/M plot should demonstrate a series of straight lines parallel to each other in the high-field region, with the one at T_C going through the origin. The slopes of the M^2 vs H/M curves reveal the order of the transition: A positive slope suggests a second-order (continuous) phase transition, whereas a negative slope implies a first-order (discontinuous) one [40]. Figures 3(c) and 3(d) show the Arrott plots of M^2 vs H/M for $H//ab$ and $H//c$ respectively, with positive slopes indicating second-order phase transitions. However, the M^2 vs H/M curves are nonlinear and not parallel, suggesting that the Arrott plot associated with the mean-field model cannot explain the critical behaviors of Cr_3Te_4.

In general, the magnetic behaviors are described by the Arrott-Noakes equation of states [41],

$$(H/M)^{1/\gamma} = (T - T_C)/T_C + (M/M_1)^{1/\beta}, \qquad (1)$$

where β and γ are the critical exponents, and the M_1 is constant. The critical exponents can be determined by the following functions [42]:

$$M_s(T) = M_0(-\varepsilon)^\beta, \quad \varepsilon < 0, T < T_C, \qquad (2)$$

$$\chi_0(T)^{-1} = (h_0/M_0)\varepsilon^\gamma, \quad \varepsilon > 0, T > T_C, \qquad (3)$$

$$M = DH^{1/\delta}, \quad \varepsilon = 0, T = T_C, \qquad (4)$$

where $\varepsilon = (T - T_C)/T_C$ is the reduced temperature, h_0/M_0, M_0, and D are critical amplitudes. The critical exponents β, γ, and δ are corresponding to the spontaneous magnetization M_S, initial magnetic susceptibility χ_0, and isothermal $M(H)$ at T_C, respectively. Since the traditional Arrott plot cannot
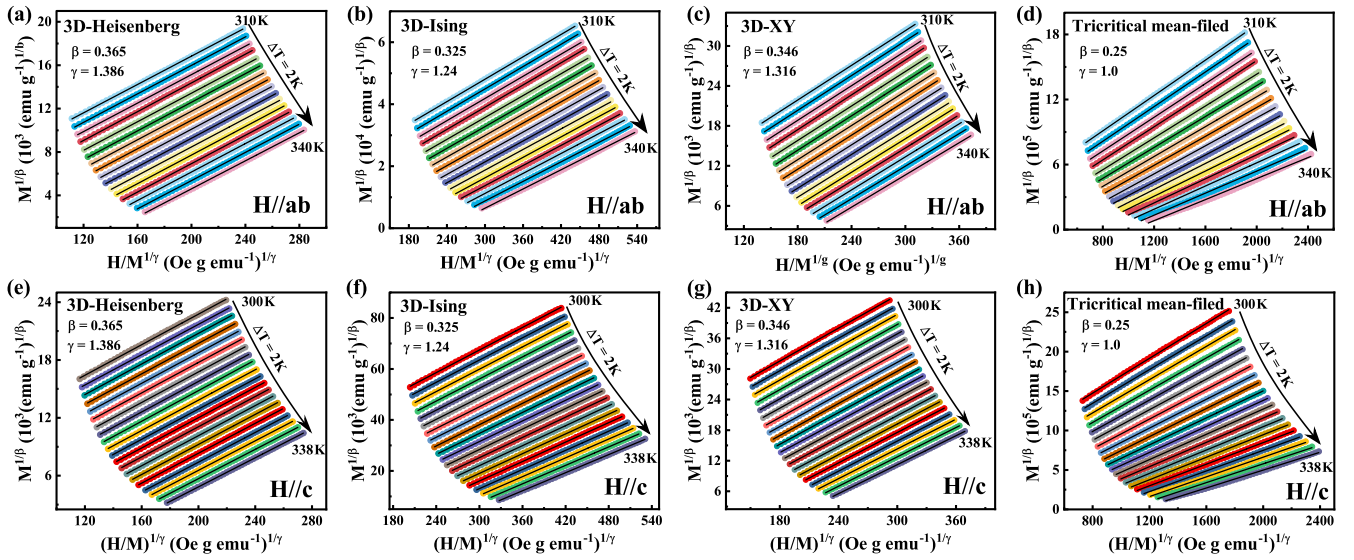
FIG. 4. Modified Arrott plots (MAPs) of $M^{1/\beta}$ vs $H/M^{1/\gamma}$ for different theoretical models including 3D-Heisenberg, 3D-Ising, 3D-XY, and tricritical mean-field models. [(a)–(d)] Those for $H//ab$, and [(e)–(h)] those for $H//c$.

describe the critical behaviors of Cr_3Te_4, the modified Arrott plot (MAP) of $M^{1/\beta}$ vs $(H/M)^{1/\gamma}$ is adopted. In order to obtain the critical parameters, four common models, 3D-Heisenberg, 3D-Ising, 3D-XY, and tricritical mean-field models, have been opted to construct the MAPs for both $H//ab$ and $H//c$. As can be observed, all of the $M^{1/\beta}$ vs $(H/M)^{1/\gamma}$ in Fig. 4 are quasistraight in the high-field region. Thus, the optimum model for describing the critical behaviors of Cr_3Te_4 still needs to be determined. To choose the best model representing spin interactions in Cr_3Te_4, we utilized the normalized slopes (NS) technique defined as $NS = S(T)/S(T_C)$ [where $S(T)$ is the slope of single $M^{1/\beta}$ vs $(H/M)^{1/\gamma}$]. The NS should be near "1" if the MAP displays a series of entire parallel lines regardless of temperature. As seen in Figs. 5(a) and 6(a), the 3D-Heisenberg model is the most suitable initial one for

$H//ab$ and $H//c$. A rigorous iterative procedure is employed to identify the proper values of β and γ. By linear extrapolation from the high-field region to the intercepts with the axes $M^{1/\beta}$ and $(H/M)^{1/\gamma}$, the initial values of $M_S(T)$ and $\chi_0^{-1}(T)$ with $H//ab$ and $H//c$ are determined from the MAPs based on 3D-Heisenberg model. New MAPs are constructed using the newly obtained values of β and γ. This process is repeated until β and γ are stable. Figures 5(b) and 6(b) show the final $M_S(T)$ and $\chi_0^{-1}(T)$ with solid fitting curves for $H//ab$ and $H//c$, respectively. Using this iterative method, the critical exponents $\beta = 0.365(5)$ with $T_C = 320.335(5)$ K and $\gamma = 1.212(9)$ with $T_C = 320.642(2)$ are obtained for $H//ab$. Meanwhile, $\beta = 0.370(3)$ with $T_C = 313.955(8)$ K and $\gamma = 1.329(1)$ with $T_C = 314.246(4)$ K are acquired for $H//c$. Figures 5(c) and 6(c) show isothermal magnetization $M(H)$ at
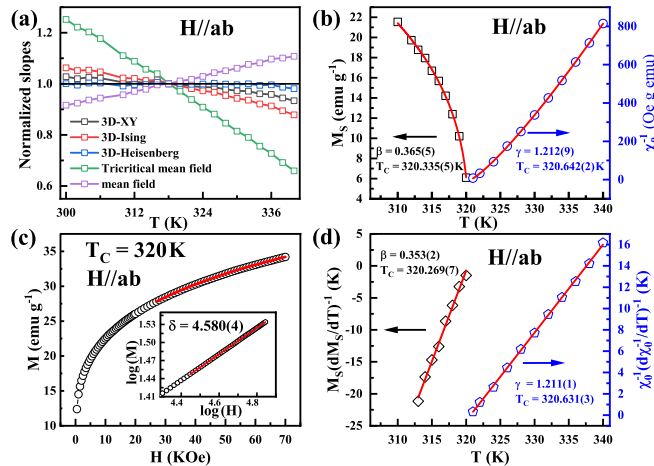

FIG. 5. The fitting for $H//ab$: (a) NS vs T for different models. (b) M_S (left) and χ_0^{-1} (right) with the fitting curves (red). (c) The initial $M(H)$ at $T_C = 320$ K with that on log-log scale in the inset. (d) KF plot for $M_S(dM_S/dT)^{-1}$ (left) and $\chi_0^{-1}(d\chi_0^{-1}/dT)^{-1}$ (right) with fitted lines.
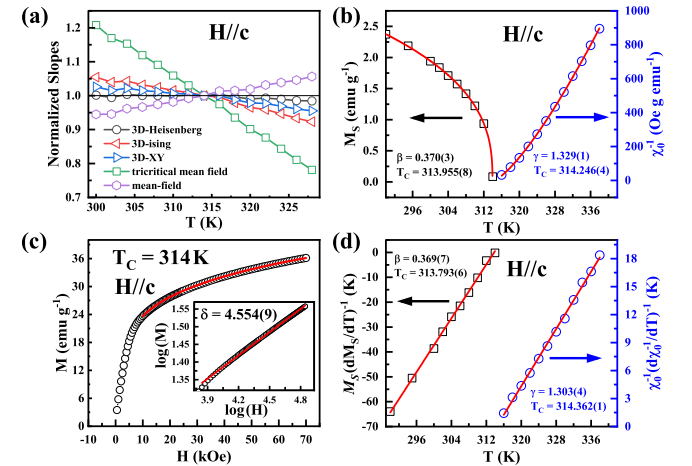
FIG. 6. The fitting for $H//c$. (a) NS vs T for different models. (b) M_S (left) and χ_0^{-1} (right) with the fitting curves (red). (c) The initial $M(H)$ at $T_C = 314$ K with that on log-log scale in the inset. (d) KF plot for $M_S(dM_S/dT)^{-1}$ (left) and $\chi_0^{-1}(d\chi_0^{-1}/dT)^{-1}$ (right) with fitted lines.

critical temperatures $T_C = 320$ K for $H//ab$ and $T_C = 314$ K for $H//c$, respectively, with the insets plotted the same curves on a log-log scale. Equation (4) can be used to obtain the third critical exponent $\delta = 4.580(4)$ for $H//ab$ and $\delta = 4.554(9)$ for $H//c$. The exponents can be examined using the Widom scaling relation, which provides the following relationship between β, γ, and δ [43]:

$$\delta = 1 + \frac{\gamma}{\beta}. \tag{5}$$

Using the β and γ from the MAP iterative method, we found $\delta = 4.318(8)$ for $H//ab$ and $\delta = 4.588(7)$ for $H//c$, confirming the self-consistency and reliability of the derived critical exponents.

Alternatively, the critical exponents can be further examined by the Kouvel-Fisher (KF) technique [44],

$$\frac{M_S(T)}{dM_S(T)/dT} = \frac{T_C - T}{\beta}, \tag{6}$$

$$\frac{\chi_0^{-1}(T)}{d\chi_0^{-1}(T)/dT} = \frac{T_C - T}{\gamma}. \tag{7}$$

The $M_S(T)/[dM_S(T)/dT]$ and $\chi_0^{-1}(T)/[d\chi_0^{-1}(T)/dT]$ are linear in relationship with temperature, with slopes $1/\beta$ and $1/\gamma$ respectively. As shown in Fig. 5(d), the linearly fitting gives $\beta = 0.353(2)$ with $T_C = 320.269(7)$ K and $\gamma = 1.211(1)$ with $T_C = 320.631(3)$ K for $H//ab$. Meanwhile, as plotted in Fig. 6(d), $\beta = 0.369(7)$ with $T_C = 313.793(6)$ K and $\gamma = 1.303(4)$ with $T_C = 314.362(1)$ K are acquired for $H//c$. The values of β and γ obtained from the KF method are consistent with those extracted by the MAP iterative method, further confirming the reliability of these obtained critical exponents.

It is important to verify that these critical exponents fulfill the magnetic equation of state in the asymptotic critical region. The magnetic equation of state is presented as follows:

$$M(H, \varepsilon) = \varepsilon^\beta f_\pm(H/\varepsilon^{\beta+\gamma}), \tag{8}$$

where f_+ ($T > T_C$) and f_- ($T < T_C$) are the regular functions. Equation (8) can also be stated in terms of renormalized magnetization $m = \varepsilon^{-\beta} M(H, \varepsilon)$ and renormalized field $h = \varepsilon^{-(\beta+\gamma)} H$ as

$$m = f_\pm(h). \tag{9}$$

Equation (9) predicts that for the proper selection of critical exponents, the normalized $m(h)$ curves should split into two distinct branches for $T > T_C$ and $T < T_C$. As shown in Figs. 7(a) and 7(b), all $m(h)$ curves around T_C collapse onto two distinct branches. Alternatively, the accuracy of critical exponents and T_C is confirmed more rigorously by plotting m^2 against h/m. The inset of Figs. 7(a) and 7(b) depict m^2 vs h/m in which all curves are split into two universal curves: one for $T > T_C$ and another for $T < T_C$, indicating that interactions in the critical regime are properly renormalized using a scaling state equation. Figures 7(c) and 7(d) show the final MAPs obtained with the values $\beta = 0.365(5)$ and $\gamma = 1.212(9)$ for $H//ab$, and $\beta = 0.370(3)$ and $\gamma = 1.329(1)$ for $H//c$, respectively. The final MAPs show that all the lines in the high-field region are reasonably straight and that one line crosses the origin at $T_C = 320$ K for $H//ab$ and $T_C = 314$ K for $H//c$. The critical exponents of Cr_3Te_4 single crystal
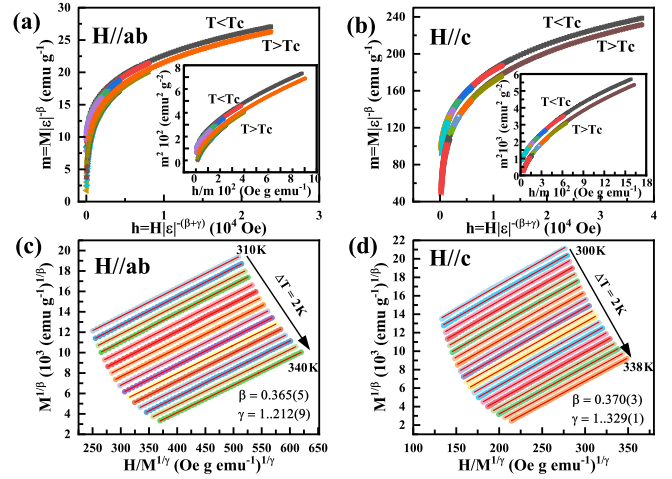

FIG. 7. [(a),(b)] Scaling plot of normalized $m(h)$ curves for $H//ab$ and $H//c$ (the insets show scaling plots of m^2 vs h/m). [(c),(d)] MAPs with the obtained critical exponents on liner scale in high-field region for $H//ab$ and $H//c$.

determined using various techniques are provided in Table I for comparison with those of related materials and theoretical models. The critical exponents β for both $H//ab$ and $H//c$ are close to the 3D-Heisenberg model. However, γ for $H//ab$ is close to the 3D-Ising model and that for $H//c$ is close to the 3D-XY model, which indicates anisotropic magnetic interactions in this system. The critical exponents of Cr_3Te_4 single crystal cannot be described under a single universality class, which is similar to other compounds of the Cr_xTe_y family listed in Table I. This result demonstrates multiple and complex magnetic interactions in Cr_3Te_4, as well as in other Cr_xTe_y. The universality class of the magnetic phase transition depends on the exchange interaction $J(r)$. According to the renormalization group theory, the exchange interaction decays as $J(r) \sim 1/r^{d+\sigma}$ for long range, and $J(r) \sim e^{-r/b}$ for short range (where d is spatial dimensionality, σ is a positive constant, b is a spatial scaling factor, and r is the spatial distance). The $J(r)$ is related to γ and σ as [42,45]

$$\gamma = 1 + \frac{4}{d}\frac{n+2}{n+8}\Delta\sigma + \frac{8(n+2)(n-4)}{d^2(n+8)^2}$$

$$\times \left[1 + \frac{2G(\frac{d}{2})(7n+20)}{(n-4)(n+8)}\right]\Delta\sigma^2 \tag{10}$$

where n is the spin dimensionality, and $\Delta\sigma = \sigma - \frac{d}{2}$, $G(\frac{d}{2}) = 3 - \frac{1}{4}(\frac{d}{2})^2$. The parameter in the above expression is adjusted for particular values of $\{d : n\}$ to produce values similar to those obtained experimentally, $\gamma = 1.212(9)$ for $H//ab$ and $\gamma = 1.329(1)$ for $H//c$. The process is repeated with a different set of $\{d : n\}$. It was observed that for $\{d : n\} = \{3 : 1\}$ and $\sigma = 1.863(3)$, the exponent γ approaches experimentally obtained values for in-plane ($H//ab$). According to the following expressions: $\upsilon = \gamma/\sigma$, $\alpha = 2 - \upsilon d$, $\beta = (2 - \alpha - \gamma)/2$, $\delta = 1 + \gamma/\beta$, the other exponents are computed as $\beta = 0.369(8)$ and $\delta = 4.277(1)$, which match the experimental values, showing that the finding is reliable. Meanwhile, for $H//c$, $\{d : n\} = \{3 : 2\}$, and $\sigma = 1.934(2)$, the exponents

TABLE I. Comparison of critical exponents of Cr_3Te_4 single crystal, related Cr_xTe_y compounds, and different theoretical models [modified Arrott plot (MAP), Kouvel-Fisher (KF) technique, and critical isotherm (CI) analysis].

Composition	Reference	Technique	T_C (K)	β	γ	δ
		MAP	320.335(5)	0.365(5)	1.212(9)	4.318(8)
Cr_3Te_4 $H//ab$	This paper	KF	320.269(7)	0.353(2)	1.211(1)	4.429(4)
		CI				4.580(4)
		MAP	313.955(8)	0.370(3)	1.329(1)	4.588(7)
Cr_3Te_4 $H//c$	This paper	KF	313.793(6)	0.369(7)	1.303(4)	4.525(1)
		CI				4.554(9)
Mean-field		Theory		0.5	1	3
3D-XY		Theory		0.345	1.316	4.81
3D-Heisenberg		Theory		0.365	1.386	4.8
3D-Ising		Theory		0.325	1.24	4.82
Tricritical mean field		Theory		0.25	1.0	5
m-$Cr_5Te_8(H//c)$	[17]	MAP	222.13(4)	0.327(4)	1.26(1)	4.85(1)
$Cr_{0.62}Te$ $H//c$	[16]	MAP	230.76(9)	0.314(7)	1.83(2)	6.83(7)
$Cr_4Te_5(H//ab)$	[19]	MAP	319.06(9)	0.388(4)	1.290(8)	4.32(3)
$Cr_5Te_6(H//ab)$	[20]	MAP	340.73(4)	0.485(3)	1.202(5)	3.52(3)

$\beta = 0.366(3)$ and $\delta = 4.628(2)$ are in good agreement with our experimentally determined values for out-of-plane ($H//c$). Consequently, the calculations reveal that the interaction decays with distance as $J(r) \sim r^{-4.863}$ for in-plane ($H//ab$) and $J(r) \sim r^{-4.934}$ for out-of-plane ($H//c$), respectively. It is noticed that the magnetic coupling of the monoclinic Cr_5Te_8 (m-Cr_5Te_8) is also of the Ising-like type for $H//c$ [17]. However, the critical behavior of Cr_4Te_5 for $H//ab$ is of a 3D-Heisenberg type, whereas Cr_5Te_6 for $H//ab$ is of a 3D-Ising one [19,20]. The variety of universality classes confirms complex magnetic interactions in Cr_xTe_y.

Since the Cr_3Te_4 possesses multiple phase transitions and complex magnetic structures, it is necessary to construct the $H - T$ phase diagrams for $H//ab$ and $H//c$. Based on low-field MAPs and $M(T)$ curves in Figs. 8(a)–8(d), the transition boundaries can be distinguished by the inflection points. Figures 9(a) and 9(b) show the $H - T$ phase diagrams of Cr_3Te_4

single crystal for $H//ab$ and $H//c$, respectively. As shown by the $M(T)$ curves in Figs. 8(c) and 8(d), an AFM ordering occurs at $T_N \sim 90$ K. However, the FM behavior remains below T_N, which suggests the coexistence of AFM and FM phases. The neutron diffraction has demonstrated the FM coupling along the a axis and AFM coupling along the ($\vec{b} + \vec{c}$) direction [46]. The spins of Cr1 and Cr2 are respectively arranged at angles of $38°$ and $30°$ with the a axis, as shown in the left insets of Figs. 9(a) and 9(b) [46]. As illustrated in Fig. 1(a), Cr_3Te_4 can be regarded as $(Cr1)^{3+}Te_2$ with intercalated 50% $(Cr2)^{2+}$ atoms {i.e., $[(Cr1)^{3+}]_2[(Cr2)^{2+}]_1Te_4$}, where $(Cr1)^{3+}$ $(3d^3)$ loses more electrons than $(Cr2)^{2+}$ $(3d^4)$ [33,47]. Therefore, there are two different layers of Cr1 and Cr2, respectively. The AFM coupling is suggested to originate from the $d - d$ direct exchange between Cr atoms (Cr1-Cr1 and Cr2-Cr2). The FM interaction stems from two couplings: the $d - p - d$ super exchange between the intralayered near-$90°$ Cr1-Te-Cr1 (or Cr2-Te-Cr2) and double exchange between interlayered Cr1-Te-Cr2 [47,48]. The nearest Cr-Te-Cr pairs form the super exchange for the intralayer Cr atoms, which favors the in-plane FM coupling. For the interlayered Cr atoms,
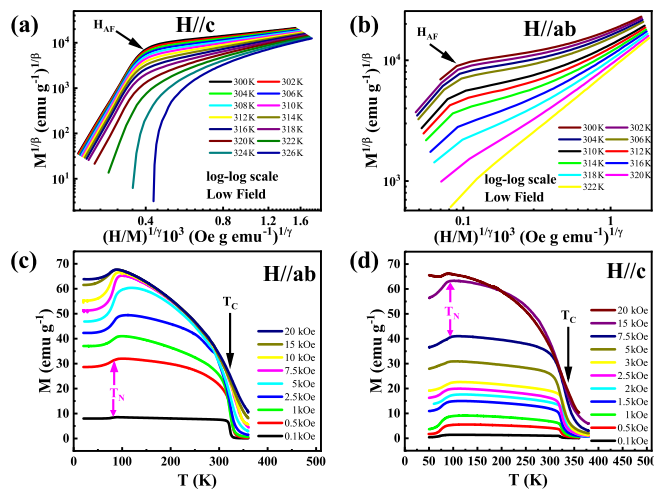

FIG. 8. MAPs on log-log scales based on the obtained critical exponents in lower-field regions for (a) $H//ab$ and (b) $H//c$. $M(T)$ curves under different field for (c) $H//ab$ and (d) $H//c$.
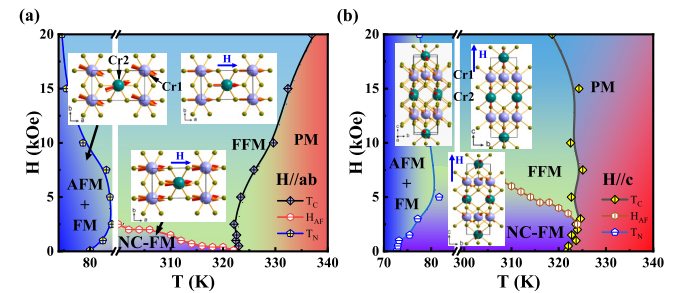

FIG. 9. [(a),(b)] $H - T$ phase diagrams of Cr_3Te_4 single crystal for $H//ab$ and $H//c$ (AFM, FM, NC-FM, FFM, and PM are on behalf of the antiferromagnetic, ferromagnetic, noncollinear ferromagnetic, forced ferromagnetic, and paramagnetic phases). The insets show the magnetic structures for (a) $H//ab$ and (b) $H//c$.

the double exchange dominates the nearest Cr1-Te-Cr2 pair, which enhances the out-of-plane FM coupling. However, the direct exchange AFM coupling competes with these two FM couplings. These three kinds of magnetic couplings [direct exchange (AFM), super exchange (FM), and double exchange (FM)] collectively result in the complex coexistence of AFM and FM phases in Cr_3Te_4. Under a lower field ($H < H_S$), as the temperature increases, the AFM coupling along ($\vec{b} + \vec{c}$) direction is suppressed, which results in the appearance of a noncollinear FM (NC-FM) state, as illustrated in the bottom insets of Figs. 9(a) and 9(b) [9,49]. This indicates that the two kinds of Cr ions in Cr_3Te_4 have strong magnetic interaction with each other, which cannot ordered independently. The NC-FM state is resulted from the strong magnetic interaction between these two kinds of Cr ions. Under higher field ($H > H_S$), both spins of Cr1 and Cr2 are polarized into the forced FM (FFM) state, as shown in the right insets of Figs. 9(a) and 9(b). Therefore, the multiple phases and magnetic structures in Cr_3Te_4 are resulted from variable magnetic interactions, including intralayer super exchange, interlayer double exchange, and direct exchange. The Cr_xTe_y, hosting complex magnetic phases and spin configurations, proves a platform to investigate the multiple magnetic interactions and couplings.

IV. CONCLUSIONS

In conclusion, the magnetic properties and critical behaviors of Cr_3Te_4 single crystal with intrinsic room-temperature ferromagnetism have been thoroughly explored for $H//ab$ and $H//c$. In contrast to the perpendicular anisotropy of the Cr_3Te_4 thin film, the magnetization study reveals a field-dependent anisotropic FM ordering with the easy axis within the ab plane in Cr_3Te_4 single crystal. The critical exponents obtained through the critical behavior analysis in the vicinity of the FM-PM transition are $\beta = 0.365(5)$, $\gamma = 1.212(9)$, $\delta = 4.580(4)$ for $H//ab$, and $\beta = 0.370(3)$, $\gamma = 1.329(1)$, $\delta = 4.554(9)$ for $H//c$. The obtained critical exponents for $H//ab$ and $H//c$ indicate strong anisotropic and multiple magnetic interactions in Cr_3Te_4 single crystal. Moreover, the obtained $J(r) \sim r^{-4.863}$ for $H//ab$ and $J(r) \sim r^{-4.934}$ for $H//c$ suggest that the magnetic interactions lie between a long-range and short-range magnetic interaction. The $H - T$ phase diagrams for $H//ab$ and $H//c$ are constructed, which unveil the coexistence of FM, AFM, NC-FM phases at low temperature and the field-dependent anisotropic FM state at room temperature. The multiple phases and variable magnetic structures in Cr_3Te_4 are resulted from the competition between the intralayer super exchange, interlayer double exchange, and direct exchange.

[1] N. D. Mermin and H. Wagner, Phys. Rev. Lett. **17**, 1133 (1966).

[2] B. Huang, G. Clark, E. Navarro-Moratalla, D. R. Klein, R. Cheng, K. L. Seyler, D. Zhong, E. Schmidgall, M. A. McGuire, D. H. Cobden et al., Nature (London) **546**, 270 (2017).

[3] C. Gong, L. Li, Z. Li, H. Ji, A. Stern, Y. Xia, T. Cao, W. Bao, C. Wang, Y. Wang et al., Nature (London) **546**, 265 (2017).

[4] Y. Deng, Y. Yu, Y. Song, J. Zhang, N. Z. Wang, Z. Sun, Y. Yi, Y. Z. Wu, S. Wu, J. Zhu et al., Nature (London) **563**, 94 (2018).

[5] M. Baranava, D. Hvazdouski, V. Skachkova, V. Stempitsky, and A. Danilyuk, Mater. Today **20**, 342 (2020).

[6] V. Carteaux, G. Ouvrard, J. Grenier, and Y. Laligant, J. Magn. Magn. Mater. **94**, 127 (1991).

[7] H. Xiao, M.-J. Mi, and Y.-L. Wang, Acta. Phys. Sin. **70**, 127503 (2021).

[8] N.-S. Liu, C. Wang, and W. Ji, Acta. Phys. Sin. **71**, 127504 (2022).

[9] B. Tang, X. Wang, M. Han, X. Xu, Z. Zhang, C. Zhu, X. Cao, Y. Yang, Q. Fu, J. Yang et al., Nat. Electron. **5**, 224 (2022).

[10] H. Wu, W. Zhang, L. Yang, J. Wang, J. Li, L. Li, Y. Gao, L. Zhang, J. Du, H. Shu et al., Nat. Commun. **12**, 5688 (2021).

[11] C. Li, K. Liu, C. Jin, D. Jiang, Z. Jiang, T. Wen, B. Yue, and Y. Wang, Inorg. Chem. **61**, 11923 (2022).

[12] V. Kanchana, G. Vaitheeswaran, and M. Rajagopalan, J. Magn. Magn. Mater. **250**, 353 (2002).

[13] T. Eto, M. Ishizuka, S. Endo, T. Kanomata, and T. Kikegawa, J. Alloys Compd. **315**, 16 (2001).

[14] N. Kang, W. Wan, Y. Ge, and Y. Liu, Front. Phys. **16**, 63506 (2021).

[15] M. Huang, S. Wang, Z. Wang, P. Liu, J. Xiang, C. Feng, X. Wang, Z. Zhang, Z. Wen, H. Xu et al., ACS Nano **15**, 9759 (2021).

[16] Y. Liu and C. Petrovic, Phys. Rev. B **96**, 134410 (2017).

[17] X. Zhang, T. Yu, Q. Xue, M. Lei, and R. Jiao, J. Alloys Compd. **750**, 798 (2018).

[18] M. Yamaguchi and T. Hashimoto, J. Phys. Soc. Jpn. **32**, 635 (1972).

[19] L.-Z. Zhang, A.-L. Zhang, X.-D. He, X.-W. Ben, Q.-L. Xiao, W.-L. Lu, F. Chen, Z. Feng, S. Cao, J. Zhang, and J.-Y. Ge, Phys. Rev. B **101**, 214413 (2020).

[20] L.-Z. Zhang, Q.-L. Xiao, F. Chen, Z. Feng, S. Cao, J. Zhang, and J.-Y. Ge, J. Magn. Magn. Mater. **546**, 168770 (2022).

[21] M. Bian, L. Zhu, X. Wang, J. Choi, R. V. Chopdekar, S. Wei, L. Wu, C. Huai, A. Marga, Q. Yang et al., Adv. Mater. **34**, 2200117 (2022).

[22] L. Zhou, J. Chen, X. Chen, B. Xi, Y. Qiu, J. Zhang, L. Wang, R. Zhang, B. Ye, P. Chen et al., ACS Appl. Mater. Inter. **12**, 25135 (2020).

[23] J. Chen, L. Wang, M. Zhang, L. Zhou, R. Zhang, L. Jin, X. Wang, H. Qin, Y. Qiu, J. Mei *et al.*, Nano Lett. **19**, 6144 (2019).

[24] D. Zhao, L. Zhang, I. A. Malik, M. Liao, W. Cui, X. Cai, C. Zheng, L. Li, X. Hu, D. Zhang *et al.*, Nano Res. **11**, 3116 (2018).

[25] Y. Liu and C. Petrovic, Phys. Rev. B **98**, 195122 (2018).

[26] Z. Z. Jiang, X. Luo, J. Yan, J. J. Gao, W. Wang, G. C. Zhao, Y. Sun, J. G. Si, W. J. Lu, P. Tong, X. B. Zhu, W. H. Song, and Y. P. Sun, Phys. Rev. B **102**, 144433 (2020).

[27] J. Liu, B. Ding, J. Liang, X. Li, Y. Yao, and W. Wang, ACS Nano **16**, 13911 (2022).

[28] J. H. Jeon, H. R. Na, H. Kim, S. Lee, S. Song, J. Kim, S. Park, J. Kim, H. Noh, G. Kim *et al.*, ACS Nano **16**, 8974 (2022).

[29] B. Li, X. Deng, W. Shu, X. Cheng, Q. Qian, Z. Wan, B. Zhao, X. Shen, R. Wu, S. Shi *et al.*, Mater. Today **57**, 66 (2022).

[30] Q. Wu, R. Liu, Z. Qiu, D. Li, J. Li, X. Wang, and G. Ding, Phys. Chem. Chem. Phys. **24**, 24873 (2022).

[31] R. Chua, J. Zhou, X. Yu, W. Yu, J. Gou, R. Zhu, L. Zhang, M. Liu, M. B. Breese, W. Chen *et al.*, Adv. Mater. **33**, 2103360 (2021).

[32] Y. Wang, S. Kajihara, H. Matsuoka, B. K. Saika, K. Yamagami, Y. Takeda, H. Wadati, K. Ishizaka, Y. Iwasa, and M. Nakano, Nano Lett. **22**, 9964 (2022).

[33] A. L. Coughlin, D. Xie, X. Zhan, Y. Yao, L. Deng, H. Hewa-Walpitage, T. Bontke, C.-W. Chu, Y. Li, J. Wang, H. A. Fertig, and S. Zhang, Nano Lett. **21**, 9517 (2021).

[34] C. Zhang, C. Liu, J. Zhang, Y. Yuan, Y. Wen, Y. Li, D. Zheng, Q. Zhang, Z. Hou, G. Yin *et al.*, Adv. Mater. **35**, 2205967 (2023).

[35] E. Bertaut, G. Roult, R. Aleonard, R. Pauthenet, M. Chevreton, and R. Jansen, J. Phys. France **25**, 582 (1964).

[36] S. Ohta, A. Fujii, and S. Anzai, J. Phys. Soc. Jpn. **52**, 1765 (1983).

[37] S. Ohta, T. Kaneko, and H. Yoshida, J. Magn. Magn. Mater. **163**, 117 (1996).

[38] H. Ipser, K. L. Komarek, and K. O. Klepp, J. Less-Common Met. **92**, 265 (1983).

[39] Y. Wang, J. Yan, J. Li, S. Wang, M. Song, J. Song, Z. Li, K. Chen, Y. Qin, L. Ling, H. Du, L. Cao, X. Luo, Y. Xiong, and Y. Sun, Phys. Rev. B **100**, 024434 (2019).

[40] L. Zhang, Acta. Phys. Sin. **67**, 137501 (2018).

[41] A. Arrott, Phys. Rev. **108**, 1394 (1957).

[42] M. E. Fisher, Rep. Prog. Phys. **30**, 615 (1967).

[43] B. Widom, J. Chem. Phys. **43**, 3898 (1965).

[44] J. S. Kouvel and M. E. Fisher, Phys. Rev. **136**, A1626 (1964).

[45] M. E. Fisher, S.-k. Ma, and B. Nickel, Phys. Rev. Lett. **29**, 917 (1972).

[46] A. F. Andresen, Acta Chem. Scand. **24**, 3495 (1970).

[47] X. Zhang, B. Wang, Y. Guo, Y. Zhang, Y. Chen, and J. Wang, Nanoscale Horiz. **4**, 859 (2019).

[48] Q. Liu, Y. Wang, Y. Zhao, Y. Guo, X. Jiang, and J. Zhao, Adv. Funct. Mater. **32**, 2113126 (2022).

[49] Z.-L. Huang, W. Kockelmann, M. Telling, and W. Bensch, Solid State Sci. **10**, 1099 (2008).